Thermochimica Acta 505 (2010) 41–46

Contents lists available at ScienceDirect

Thermochimica Acta

journal homepage: www.elsevier.com/locate/tca

Isochronal and isothermal crystallization kinetics of amorphous Fe-based alloys

J.T. Zhang[a], W.M. Wang[a,b,*], H.J. Ma[a], G.H. Li[a], R. Li[a], Z.H. Zhang[a]

[a] Key Laboratory for Liquid-Solid Structural Evolution and Processing of Materials, Ministry of Education, Shandong University, Jinan 250061, China
[b] Key Lab of Metastable Materials Science & Technology, Yanshan University, Qinhuangdao 066004, China

ARTICLE INFO

Article history:
Received 17 December 2009
Received in revised form 24 March 2010
Accepted 31 March 2010
Available online 8 April 2010

Keywords:
Crystallization kinetics
Differential scanning calorimetry
Activation energy

ABSTRACT

Using the differential scanning calorimetry (DSC), the isochronal and isothermal crystallization kinetics of amorphous $Fe_{61}Co_{9-x}Zr_8Mo_5W_xB_{17}$ ($x=0$ and 2) ribbons was investigated by the Kissinger equation and by the Kolmogorov–Johnson–Mehl–Avrami and Ranganathan–Heimendahl equations, respectively. The results show that tungsten can improve the activation energy E_1^K for the first crystallization in the isochronal annealing process and activation energy E_n for the nucleation in the isothermal annealing process, which can be ascribed to the dissolution of tungsten in the amorphous phase. Meanwhile, tungsten can decrease the activation energy E_2^K for the second crystallization in the isochronal annealing process and growth activation energy E_g in the isothermal annealing process, which is possibly associated with the formation of W-rich compound after the early nucleation process.

1. Introduction

During the past four decades, Fe-based glasses have been extensively investigated due to not only their potential mechanical and magnetic applications, but also their significantly low cost. For instance, the $(Fe_{0.75}B_{0.15}Si_{0.1})_{100-x}M_x$ glasses (M = Nb, Zr) have a high saturated magnetic flux density [1] and the $Fe_{61}Cr_{15}C_{15}Mo_{14}Co_7B_6Y_2$ glass bears an ultra-high fracture strength [2].

Since Fe–Co–(Zr, Nb, Ta)–(Mo, W)–B bulk metallic glasses (BMGs) were firstly discovered in 1997 [3,4], a number of attentions have been paid on them, especially on the $Fe_{60}Co_{10}Zr_8Mo_5W_2B_{15}$ alloy due to its high strength, high corrosion, high glass-forming ability (GFA), high thermal stability and good soft magnetic properties. Recently, the GFA, fragility, microstructure and magnetic properties of $Fe_{61}Co_{9-x}Zr_8Mo_5W_xB_{17}$ ($0 \le x \le 3$) glasses have been found to be dependent on the minor additions [5], annealing processes [6], and vacuum conditions [7].

In the metallic glasses, an amorphous phase always has a higher free energy than its crystalline counterpart, and it will transform into crystalline phases if obtaining enough additional energy. The crystallization of an amorphous phase will result in the changes of its structure and inherent properties [8]. Consequently, controlling the process of crystallization is critical to obtain the desirable microstructures and properties. Generally, the crystallization kinetics can be investigated using the techniques of differential scanning calorimetry (DSC) [9], ferromagnetic resonance [10], Mössbauer spectroscopy [11], small angle X-ray scattering [12] and electrical resistance measurements [13].

The crystallization of an amorphous alloy is generally regarded as the nucleation and growth processes of the crystalline phase in the amorphous matrix. The activation energy of nucleation and growth (E_n and E_g) can be determined by the quantitative transmission electron microscopy (TEM) [14]. E_n and E_g can also be determined by applying the crystallization kinetic theory, which is based on the variation of measured local activation energy $E_c(x)$ and Avrami exponent $n(x)$ with the crystallized volume fraction x [15–17]. However, there are few investigations on the crystallization kinetics of the Fe–Co–Zr–Mo–W–B alloys up to now. The research on the crystallization kinetics is helpful to outline the optimum annealing treatment of the Fe–Co–Zr–Mo–W–B glasses.

In our paper, the crystallization kinetics of the Fe–Co–Zr–Mo–W–B glasses has been studied using the DSC method in isochronal and isothermal annealing modes. The crystallization kinetics parameters such as the Avrami exponent and activation energies have been calculated.

2. Experimental

The master alloy ingots with the chemical compositions of $Fe_{61}Co_9Zr_8Mo_5B_{17}$ and $Fe_{61}Co_7Zr_8Mo_5W_2B_{17}$ were prepared by induction-melting the mixture of metals in high purity, except B that was added using a Fe–16.8 wt.%B master alloy. In order to guarantee the homogeneity of samples, all ingots were re-molten for at least three times.

* Corresponding author at: Key Laboratory for Liquid-Solid Structural Evolution and Processing of Materials, Ministry of Education, Shandong University, Jinan 250061, China. Tel.: +86 531 88392749; fax: +86 531 88395011.
E-mail address: weiminw@sdu.edu.cn (W.M. Wang).

0040-6031/$ – see front matter © 2010 Elsevier B.V. All rights reserved.
doi:10.1016/j.tca.2010.03.023

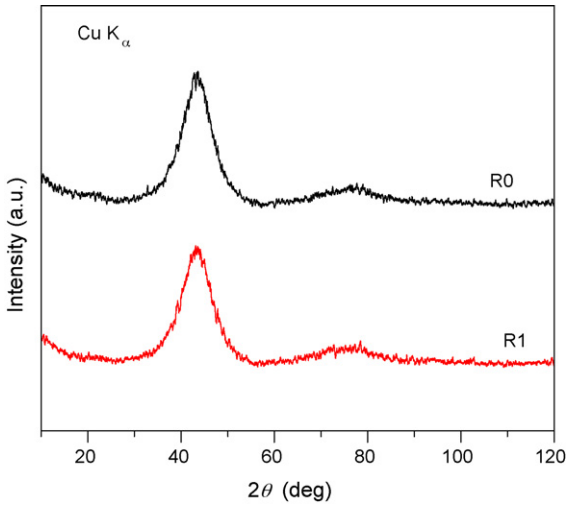

Fig. 1. XRD patterns of the as-spun R0 and R1 ribbons.

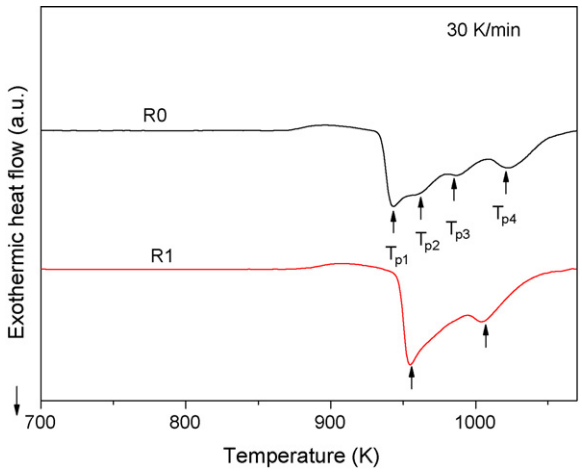

Fig. 2. Isochronal DSC curves of the amorphous as-spun R0 and R1 ribbons at a heating rate of 30 K/min.

Ribbons were obtained by single roller melt spinning using a Buehler Melt quenching apparatus (Edmund Buehler GmbH) at a wheel speed of 23 m/s in an argon atmosphere. Before melting spinning, we reduced the pressure of the casting chamber to 2.0×10^{-3} Pa using the mechanical vacuum pump and molecular vacuum pump, then input the 6.0×10^{4} Pa argon. The $Fe_{61}Co_{9-x}Zr_8Mo_5W_xB_{17}$ ribbons with $x = 0$ and 2 are labeled as R0 and R1, respectively.

The structures of the as-spun and annealed ribbons were investigated by X-ray diffraction (XRD) using a D/Max-rB diffractometer with Cu Kα radiation ($\lambda = 0.154059$ nm). The isochronal and isothermal annealing processes for the crystallization of R0 and R1 ribbons were performed on a differential scanning calorimetry (Netzsch DSC 404c) under a flow of high-purity argon atmosphere. For the isochronal annealing process, the DSC plots were recorded with the heating rates of 10, 20, 30, 40 and 50 K/min. For the isothermal annealing process, the as-spun samples were first heated up to a fixed temperature within the supercooled liquid region at a rate of 50 K/min, then held for a certain period of time until the crystallization is completed.

3. Results

The X-ray diffraction (XRD) data of the as-spun R0 and R1 ribbons are measured by Cu Kα radiation, as shown in Fig. 1. The patterns of the R0 and R1 ribbons present a fully diffuse maximum centered at $2\theta = 43.5^{\circ}$, which is typical character of the fully amorphous phase and consistent with the results by Co Kα radiation [6].

3.1. Isochronal annealing

Fig. 2 shows the isochronal DSC curves of the R0 and R1 ribbons at a heating rate of 30 K/min. There are four exothermic peaks in the DSC curve of the R0 ribbon, the temperatures of which are named as T_{p1}, T_{p2}, T_{p3} and T_{p4}, respectively. In the DSC curve of R1, there are only two exothermic peaks, locating at the higher temperatures, compared with the corresponding peaks of the R0 ribbon.

Thermal parameters such as the glass transition temperature T_g, the onset crystallization temperature T_x, the first, second, third and fourth peak temperatures T_{p1}, T_{p2}, T_{p3} and T_{p4} of the R0 and R1 ribbons at a heating rate (ν) of 30 K/min have been listed in Table 1. The changing behavior of the thermal parameters measured at $\nu = 10$, 20, 40 and 50 K/min (not shown in this paper) is similar to that at $\nu = 30$ K/min. Obviously, the DSC parameters such as T_g, T_x, T_{p1} and T_{p2} of the R1 ribbon are higher than the corresponding ones of the R0 ribbon, in other words, the thermal stability of the R1 ribbon is higher than that of R0, implying that it can improve the thermal stability by adding tungsten in the amorphous Fe–Co–Zr–Mo–B alloy.

The activation energy E^K of the crystallization can be calculated by using the Kissinger equation [18]:

$$\ln\left(\frac{\nu}{T^2}\right) = -\frac{E^K}{RT} + B, \quad (1)$$

where R is the gas constant, B is a constant and T is a specific temperature such as T_{p1}, T_{p2}, T_{p3} or T_{p4}. Based on the Kissinger equation, a straight line can be obtained by plotting $\ln(\nu/T^2)$ vs. $1/(T)$, which is shown in Fig. 3. The slope of this line stands for the value of the activation energy E^K of the corresponding reaction. For simplicity, the E^K for the first, second, third and fourth crystallization are labeled as E_1^K, E_2^K, E_3^K and E_4^K, respectively, which are listed in Table 2. The E_1^K of R0 and R1 ribbons are 414 and 480 kJ/mol, respectively. These values are higher than those of the $Fe_{81}B_{13}Si_4C_2$ ($E_1^K = 351.2$ kJ/mol) [19], $Fe_{85}B_{15}$ ($E_1^K = 294$ kJ/mol) [20], and $Fe_{76}Cr_{10}B_{14}$ ($E_1^K = 395$ kJ/mol) glasses [20], indicating that the amorphous Fe–Co–Zr–Mo–W–B alloys have a higher thermal stability. Compared with the R0 ribbon, the E_1^K of the R1 ribbon is obviously higher, which is consistent with T_x and suggesting that tungsten improves the difficulty of the primary crystallization of the ribbon. Interestingly, the R1 ribbon's E_2^K is obvious lower, but its T_{p2} is higher than the corresponding parameter of the R0 ribbon.

Table 1
Thermal parameters of the R0 and R1 ribbons at a heating rate of 30 K/min.

Sample	T_g (K)	T_x (K)	T_{p1} (K)	T_{p2} (K)	T_{p3} (K)	T_{p4} (K)
R0	853	939	943	959	986	1022
R1	867	944	955	1004	–	–

Table 2
The activation energies of the R0 and R1 ribbons calculated by using the Kissinger equation.

Sample	E_1^K (kJ/mol)	E_2^K (kJ/mol)	E_3^K (kJ/mol)	E_4^K (kJ/mol)
R0	414	666	541	308
R1	480	369	–	–

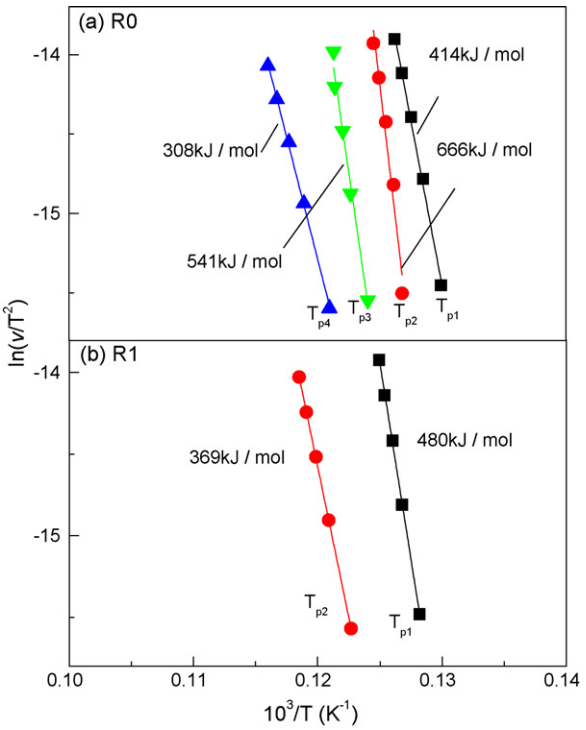

Fig. 3. Kissinger plots of $\ln(v/T^2)$ vs. $1000/T$ for the first, second, third and fourth exothermic peaks of the amorphous as-spun ribbons: (a) R0; (b) R1.

3.2. Isothermal annealing

Fig. 4 shows the XRD patterns of the R0 and R1 ribbons at different temperatures within the supercooled liquid region, ranging from 893 to 913 K and from 908 to 928 K, respectively. It indicates

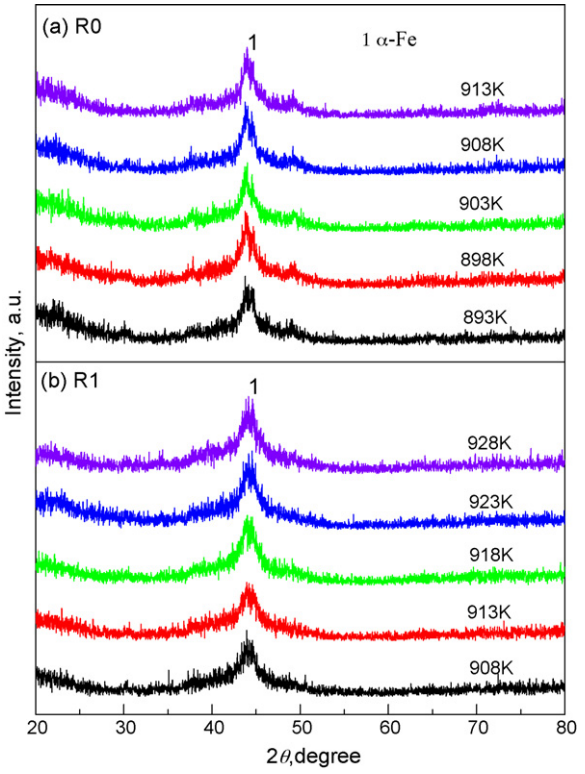

Fig. 4. XRD patterns of the samples annealed at different temperatures: (a) R0; (b) R1.

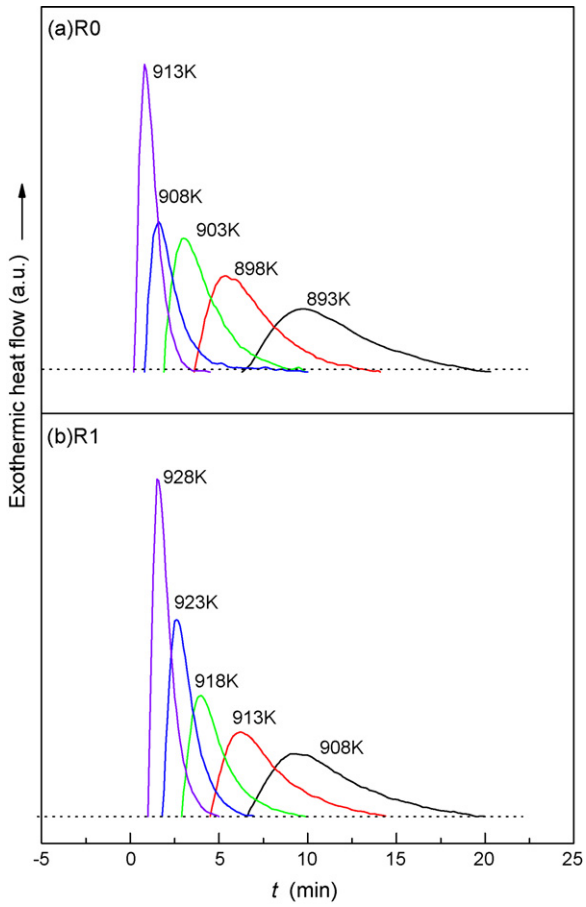

Fig. 5. Isothermal DSC curves of the as-spun ribbons at different annealing temperatures: (a) R0; (b) R1.

that the major product of the primary crystallization of the R0 and R1 ribbons is α-Fe.

Fig. 5 shows the isothermal DSC curves of the R0 and R1 ribbons at different temperatures within the supercooled liquid region, ranging from 893 to 913 K and from 908 to 928 K, respectively. In Fig. 5, there is only a single exothermal peak after passing a certain incubation period in each curve, and the incubation time τ (the time when the crystallized volume fraction up to 0.005) and the time interval Δt (the interval between the onset crystallization time t_{on} and the ending crystallization time t_{end}) reduce gradually along with increasing temperature for the same ribbon. Then the volume fraction $x(t)$ crystallized up to any time t can be calculated using the equation:

$$x(t) = \frac{A(t)}{A_{tot}}, \tag{2}$$

where $A(t)$ is the partial area of exothermic peak obtained by integrating the isothermal DSC curves from t_{on} up to time t and A_{tot} the total area of the exothermic peak. The parameters such as the incubation time τ and interval Δt of the R0 and R1 ribbons at different annealing temperatures are listed in Table 3. At the same temperature, the τ and Δt of the R1 ribbon are much higher than the corresponding parameters of the R0 ribbon, indicating a higher thermal stability of the R1 ribbon.

After the volume fraction $x(t)$ at time t has been obtained according to Eq. (2), the isothermal crystallization kinetics of the amorphous alloys can be analyzed using the Kolmogorov–Johnson–Mehl–Avrami (KJMA) equation [21]:

$$x(t) = 1 - \exp[-k(t-\tau)^n], \tag{3}$$

Table 3
The KJMA parameters such as τ, Δt of the amorphous as-spun R0 and R1 ribbons annealed at different temperatures.

Sample	Parameters at different temperatures							
	893 K	898 K	903 K	908 K	913 K	918 K	923 K	928 K
R0								
τ (min)	7.6	4.5	2.7	1.1	0.3	–	–	–
Δt (min)	27	23	13	9	4	–	–	–
R1								
τ (min)	–	–	–	7.6	5.4	3.6	2.1	1.1
Δt (min)	–	–	–	23	17	12	8	4

where k is a reaction rate constant which is a kinetics parameter depending on the annealing temperature, nucleation rate and growth rate, and n is the Avrami exponent which reflects the characteristics of nucleation and growth during crystallization.

Based on Eq. (3), we can obtain the following equation:

$$\ln[-\ln(1-x)] = \ln\ k + n\ln(t-\tau). \tag{4}$$

Therefore the KJMA plots of $\ln\ln(1-x)^{-1}$ against $\ln(t-\tau)$ of the R0 and R1 ribbons at different temperatures are shown in Fig. 6.

The local Avrami exponent $n(x)$ can be calculated by differentiating Eq. (4):

$$n(x) = \frac{\partial\ \ln\ln(1-x)^{-1}}{\partial \ln(t-\tau)}, \tag{5}$$

and the results are shown in Fig. 7. At the beginning of crystallization, the Avrami exponent rapidly increases to 2.0; in the middle stage, $n(x)$ increases slowly and tends to decrease after a maximum value, implying a decreasing nucleation rate and a three-dimensional growth; in the end stage, the Avrami exponent rapidly

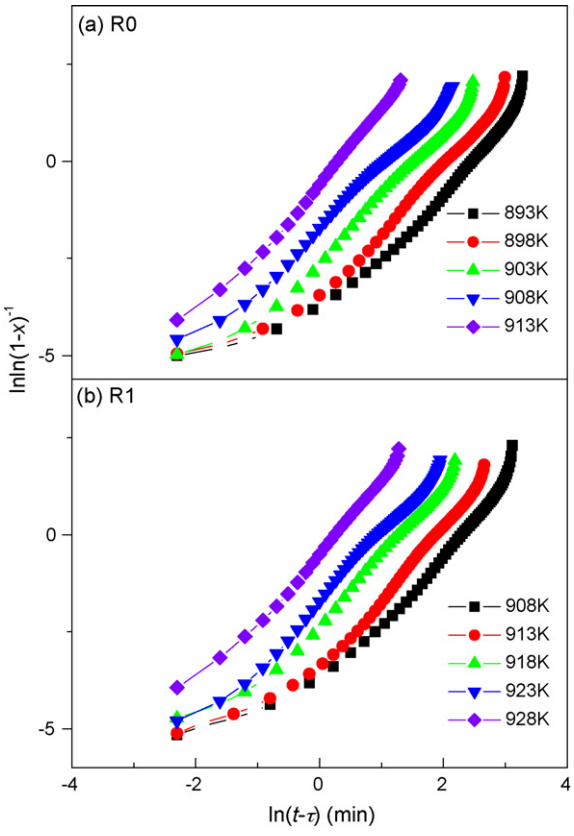

Fig. 6. KJMA plots of $\ln\ln(1-x)^{-1}$ vs. $\ln(t-\tau)$ for the crystallization at different annealing temperatures of the as-spun ribbons: (a) R0; (b) R1.

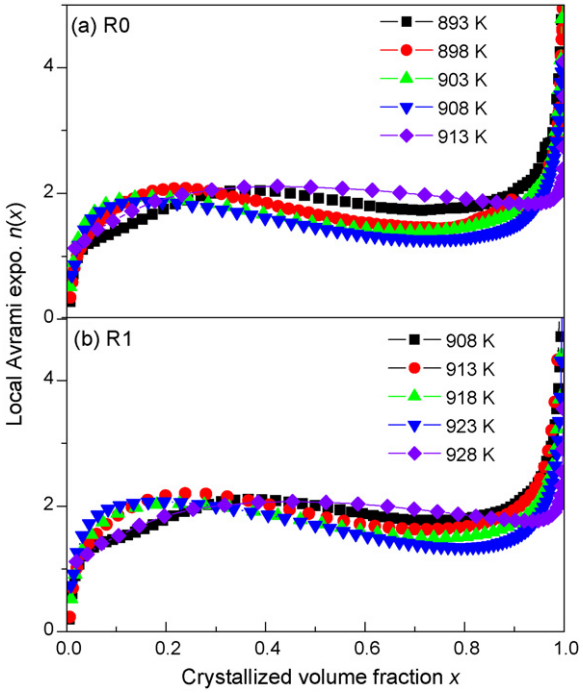

Fig. 7. Local Avrami exponent $n(x)$ vs. x of the as-spun ribbons at different annealing temperatures: (a) R0; (b) R1.

increases to above 4.0, implying an increasing nucleation rate and a three-dimensional growth. Here, the shape of $n(x)$ vs. x curves is different from that of Ni–P alloy, which shows a monotonic decrease of $n(x)$ in the end stage of $90\% < x < 100\%$, owing to only one crystallization peak in the isothermal DSC curve [17]. The rise of $n(x)$ vs. x curve of present alloys occurs in the end stage, possibly due to the start of the second crystallization, which is similar to $Al_{89}La_6Ni_5$ alloy [22].

The activation energy can also be calculated by the Arrhenius relationship equation for the isothermal annealing process [18]:

$$t(x) = t_0\ \exp\left[\frac{E^{\mathrm{A}}(x)}{RT}\right], \tag{6}$$

where $t(x)$ is the transformed time when the crystallized volume fraction reaches x, t_0 is a time constant and $E^{\mathrm{A}}(x)$ is the local activation energy. Based on Eq. (6), we can achieve the relationship of $\ln t(x)$ vs. $1/(RT)$, which can be described by a straight line and its slope is the local activation energy $E^{\mathrm{A}}(x)$. Hence, we can calculate the values of $E^{\mathrm{A}}(x)$ at different x, and then obtain the relationship of $E^{\mathrm{A}}(x)$ vs. x, as shown in Fig. 8. It can be found that the values of $E^{\mathrm{A}}(x)$ vary significantly with x, implying the changes of nucleation and growth behaviors during crystallization. At the beginning of crystallization ($x < 0.1$), $E^{\mathrm{A}}(x)$ decreases sharply with increasing x; when x exceeds 0.1, $E^{\mathrm{A}}(x)$ decreases slowly, which is similar to the Ni–P alloy [16]; at the end of crystallization ($x > 0.8$), however, another sharp decrease occurs in $E^{\mathrm{A}}(x)$, which is similar to the $Fe_{80}Si_4B_{16}$ glassy ribbon [23]. The E^{A} of the R1 ribbon is lower than that of the R0 ribbon during the entire primary crystallization ($0 < x < 0.9$), indicating that tungsten decreases the local activation energy of the amorphous $Fe_{61}Co_9Zr_8Mo_5B_{17}$ alloy in the isothermal process.

4. Discussion

The Avrami exponent n can be expressed in terms of the nucleation and growth parameters [24,25]:

$$n = a + b\omega, \tag{7}$$

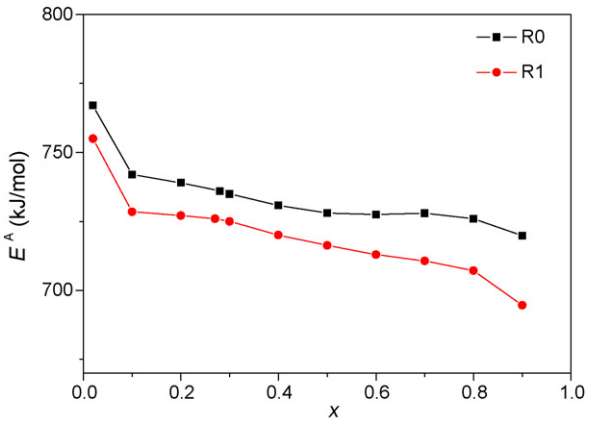

Fig. 8. Values of $E^A(x)$ of the R0 and R1 ribbons at different x.

where a is the nucleation index, b is the dimensionality of the growth with the values of 1, 2 and 3, and ω is the growth index. The nucleation index $a=0$ when the nucleation rate is zero; $0<a<1$ when the nucleation rate is decreasing with time; $a=1$ when the nucleation rate is a constant; and $a>1$ when the nucleation rate is increasing with time. The growth index $\omega=1$ stands for the linear growth, while $\omega=0.5$ stands for the parabolic growth.

In order to obtain further information in the crystallization of the Fe-based ribbons, the activation energy E^A derived by the KJMA method of the as-spun R0 and R1 ribbons can be described by the well-known equation proposed by Ranganathan and Heimendahl [15]:

$$E^A = \frac{aE_n + b\omega E_g}{a + b\omega}, \tag{8}$$

where E_n and E_g denote the activation energies for the nucleation and grain growth, respectively.

For the R0 ribbon, we can find the deviation degree of data measured at different temperatures is small at $x=0.02$ and 0.28 in Fig. 7. Moreover, different from the crystallization of the Ni–P alloy, the end part of $n(x)$ vs. x curves of R0 and R1 ribbons increases drastically possibly due to the second crystallization according to DSC curves (Fig. 2). We assume that the data with $x<0.80$ are obeying the same E_n and E_g with those deduced in the initial stage. Consequently, we choose the results at $x=0.02$, 0.28 and 0.80 to evaluate the E_n and E_g according to Eqs. (7) and (8).

Taking R0 ribbon for example, according to $n(x)$ vs. x curves in Fig. 7, the average value of Avrami exponent $\bar{n}$ at $x=0.02$, 0.28 and 0.80 is 1.11, 2.04 and 1.59, respectively. Since the growth dimensionality b are 1, 2 and 3, and linear/parabolic growth parameter $\omega=1$ and 0.5, $\bar{n}$ can be decomposed into six sets of a, b and ω considering all the possible b and ω. Based on $E^A(x)$ vs. x curves in Fig. 8, the E^A at $x=0.02$, 0.28 and 0.80 is 767, 736 and 727 kJ/mol, respectively. Substituting a, b and ω and E^A at various x into Eq. (8), we can obtain two groups of equations:

$$E^A(x_0) = \frac{aE_n + b\omega E_g}{a + b\omega}, \tag{9a}$$

$$E^A(x_1) = \frac{aE_n + b\omega E_g}{a + b\omega}, \tag{9b}$$

Table 4
The various values of a, b and ω when $x=0.02$, 0.28 and 0.8, and the roots of Eqs. (9) and (10) for R0 ribbon.

Case no.	x	E_c^A (kJ/mol)	$\bar{n}$	ω	a	b	Roots of Eq. (9) (kJ/mol)	Roots of Eq. (10) (kJ/mol)	Stardard deviation (kJ/mol)
1	0.02	767	1.11	1	0.11	1	$E_n=699$	$E_n=634$	$\sigma_n=46$
	0.28	736	2.04	1	1.04	1	$E_g=774$	$E_g=781$	$\sigma_g=5$
	0.8	727	1.59	1	0.59	1			
2	0.02	767	1.11	0.5	0.61	1	$E_n=699$	$E_n=634$	$\sigma_n=46$
	0.28	736	2.04	0.5	1.54	1	$E_g=849$	$E_g=464$	$\sigma_g=272$
	0.8	727	1.59	0.5	1.09	1			
3	0.02	767	1.11	0.5	0.61	1	$E_n=699$	$E_n=867$	$\sigma_n=119$
	0.28	736	2.04	0.5	1.54	1	$E_g=849$	$E_g=644$	$\sigma_g=145$
	0.8	727	1.59	0.5	0.59	2			
4	0.02	767	1.11	0.5	0.61	1	$E_n=561$	$E_n=867$	$\sigma_n=216$
	0.28	736	2.04	0.5	1.04	2	$E_g=917$	$E_g=644$	$\sigma_g=193$
	0.8	727	1.59	0.5	0.59	2			
5	0.02	767	1.11	0.5	0.61	1	$E_n=699$	$E_n=803$	$\sigma_n=74$
	0.28	736	2.04	0.5	1.54	1	$E_g=849$	$E_g=722$	$\sigma_g=90$
	0.8	727	1.59	0.5	0.09	3			
6	0.02	767	1.11	0.5	0.61	1	$E_n=561$	$E_n=803$	$\sigma_n=171$
	0.28	736	2.04	0.5	1.04	2	$E_g=917$	$E_g=722$	$\sigma_g=138$
	0.8	727	1.59	0.5	0.09	3			
7	0.02	767	1.11	0.5	0.61	1	$E_n=816$	$E_n=803$	$\sigma_n=9$
	0.28	736	2.04	0.5	0.54	3	$E_g=707$	$E_g=722$	$\sigma_g=11$
	0.8	727	1.59	0.5	0.09	3			
8	0.02	767	1.11	0.5	0.11	2	$E_n=699$	$E_n=634$	$\sigma_n=46$
	0.28	736	2.04	0.5	1.04	2	$E_g=774$	$E_g=781$	$\sigma_g=5$
	0.8	727	1.59	0.5	0.59	2			
9	0.02	767	1.11	0.5	0.11	2	$E_n=699$	$E_n=-15$	$\sigma_n=505$
	0.28	736	2.04	0.5	1.04	2	$E_g=774$	$E_g=872$	$\sigma_g=69$
	0.8	727	1.59	0.5	0.09	3			
10	0.02	767	1.11	0.5	0.11	2	$E_n=599$	$E_n=-15$	$\sigma_n=434$
	0.28	736	2.04	0.5	0.54	3	$E_g=917$	$E_g=872$	$\sigma_g=32$
	0.8	727	1.59	0.5	0.09	3			

Table 5
The nucleation and growth activation energies of the R0 and R1 ribbons.

Sample	ω	b			E_n (kJ/mol)	E_g (kJ/mol)
		$x=0.02$	$x=0.28$	$x=0.8$		
R0	0.5	1	3	3	816	707
R1	0.5	1	3	3	832	688

and

$$E^A(x_0) = \frac{aE_n + b\omega E_g}{a + b\omega}, \quad (10a)$$

$$E^A(x_2) = \frac{aE_n + b\omega E_g}{a + b\omega}, \quad (10b)$$

where $x_0 = 0.02$, $x_1 = 0.28$ and $x_2 = 0.80$.

All the possible values of E_n and E_g, i.e. the roots calculated from Eqs. (9) and (10), are shown in Table 4 as well as ω, a and b. Meanwhile, the standard errors σ_n and σ_g for the E_n and E_g calculated from Eqs. (9) and (10) are listed in Table 4. In Table 4, the same E_n and E_g values calculated from Eq. (9) in both Case 2 and Case 3 is owing to the same parameters for Eq. (9); but the parameters for Eq. (10) are not the same, and the E_n and E_g values calculated from Eq. (10) in Case 2 is different from those in Case 3. The general criterion to choose the optimal values from those roots of Eqs. (9) and (10) is whether the larger one of the standard deviations of E_n and E_g (σ_n and σ_g) is minimal or not. Apparently, the standard error of roots in Case 7 is smallest, indicating that the root of Eq. (9) is very close to the corresponding one from Eq. (10). Hence, the E_n and E_g of the crystallization of R0 ribbon are 816 and 707 kJ/mol, respectively. In Case 7, ω is 0.5 for $x = 0.02$, 0.28 and 0.80, suggesting that the crystallization mode is a parabolic growth. The dimensionalities b are 1, 3 and 3 for $x = 0.02$, 0.28 and 0.80, respectively, indicating that the growth dimension has an increasing tendency with x.

Using the same method, the E_n and E_g of the R1 ribbon can also be obtained. For the R1 ribbon, the E_n and E_g are 832 and 688 kJ/mol, respectively. Similar to the R0 ribbon, the ω of the R1 ribbon equals to 0.5 for $x = 0.02$, 0.27 and 0.80, suggesting a parabolic growth. The dimensionalities b are 1, 3 and 3 for $x = 0.02$, 0.27 and 0.80, respectively, being consistent with the R0 ribbon.

The calculated parameters for the crystallization of R0 and R1 ribbons are shown in Table 5. Apparently, the activation energies for nucleation E_n of R0 and R1 are larger than their E_g, which is consistent with the experimental results in $Fe_{40}Ni_{40}P_{14}B_6$ alloy measured by Ranganathan and Heimendahl [15]. The E_n of the R1 ribbon is higher, but the E_g of the R1 ribbon is lower compared with the R0 ribbon, implying tungsten can restrain the nucleation and accelerate the growth during the crystallization.

It is known that W can diffuse into the melt and then can be retained in the amorphous phase after rapidly quenching without forming any intermetallic compound [26,27]. During the isochronal and isothermal annealing processes, the b.c.c. iron will precipitate out, but the maximum equilibrant solubility of W in b.c.c. iron at room temperature is very low [28]. The nucleation of the b.c.c. iron will be controlled by the diffusion of W, which improves the activation energy for nucleation. Consequently, it is understood that the E_n of R1 ribbon is higher than that of the R0 ribbon. On the other hand, W is favorable to form the W_2B_5 compound when its content reaches 3 at.% in Fe–Co–Zr–Mo–W–B alloy [6]. When the nucleation of b.c.c. Fe is completed, the repulsive tungsten is easy to reach the critical content to form W-rich compound, and generally the compound formation is an endothermic process. Hence, W is helpful for the growth of b.c.c. iron, which can explain the lower E_g of the R1 ribbon compared with that of the R0 ribbon (Table 5). Moreover, it can be understood that the local E^A of the R1 ribbon in the isothermal annealing is lower than that of the R0 ribbon (Fig. 8).

5. Conclusions

The primary crystallization kinetics of amorphous $Fe_{61}Co_{9-x}Zr_8Mo_5W_xB_{17}$ ($x = 0$ and 2) ribbons has been investigated using both isochronal and isothermal DSC methods. The isothermal DSC experimental data show that the crystallization mode of both ribbons is one-dimensional parabolic growth at very earlier stage and three-dimensional parabolic growth afterwards. Furthermore, the activation energy, nucleation activation energy and onset temperature for the primary crystallization of the present alloys show that tungsten can restrain the nucleation of the primary crystallization, which can be ascribed to the dissolution of tungsten in the amorphous phase. Meanwhile, the related parameters indicate that tungsten can enhance the growth of the primary and secondary crystallization products, which is possibly associated with the formation of W-rich compound in the stage after the early nucleation process.

Acknowledgements

The authors acknowledge Dr. A. Gebert, Prof. J. Eckert and Prof. L. Schultz in IFW-Dresden for technical supports and the financial support from the Alexander-von-Humboldt Foundation, Germany. They also acknowledge the National Natural Science Foundation (Nos. 50871061, 50871062, 50831003 and 50631010), the Shandong Excellent Youthy Award Foundation (No. 2008BS04020), the project NCET-06-584 and the National Basic Research Program of China (973 Program) (2007CB613901) for financial supports.

References

[1] A. Inoue, B.L. Shen, Mater. Sci. Eng. A 375–377 (2004) 302.
[2] P. Pawlik, H.A. Dvaries, Scripta Mater. 49 (2003) 755.
[3] A. Inoue, T. Zhang, A. Takeuchi, Appl. Phys. Lett. 71 (1997) 464.
[4] A. Inoue, T. Zhang, H. Koshiba, A. Makino, J. Appl. Phys. 83 (1998) 6326.
[5] W.M. Wang, A. Gebert, S. Roth, U. Kuehn, L. Schultz, Intermetallics 16 (2008) 267.
[6] W.M. Wang, W.X. Zhang, A. Gebert, S. Roth, C. Mickel, L. Schultz, Metall. Mater. Trans. A 40 (2009) 511.
[7] W.M. Wang, J.T. Zhang, A. Gebert, S. Roth, L. Schultz, unpublished.
[8] M.S. Leu, J.S.C. Jang, C.C. Lin, W.K. Wang, Mater. Chem. Phys. 45 (1996) 275.
[9] J. Vazquez, P.L. Lopez-Alemany, P. Villares, R. Jimenez-Garay, J. Phys. Chem. Solids 61 (2000) 493.
[10] R.S. de Biasi, D.S. dos Santos, Mater. Sci. Forum 307 (1999) 107.
[11] M. Kopcewicz, A. Grabias, D.L. Williamson, J. Appl. Phys. 82 (1997) 1747.
[12] D.R. dos Santos, I. Torriani, F.C.S. Silva, M. Knobel, J. Appl. Crystallogr. 33 (2000) 473.
[13] D.R. dos Santos, I. Torriani, F.C.S. Slilva, M. Knobel, J. Appl. Phys. 86 (1999) 6993.
[14] C. Antonione, L. Battezzati, A. Lucci, G. Riontino, G. Venturello, Scripta Metall. 12 (1978) 1011.
[15] S. Ranganathan, M.V. Heimendahl, J. Mater. Sci. 16 (1981) 2401.
[16] K. Lu, J.T. Wang, Mater. Sci. Eng. A 133 (1991) 500.
[17] K. Lu, J.T. Wang, Sci. China A 35 (1992) 1266.
[18] L. Liu, Z.F. Wu, J. Zhang, J. Alloys Compd. 339 (2002) 90.
[19] D.M. Minic, B. Adnadevic, Thermochim. Acta 474 (2008) 41.
[20] S.D. Kaloshkim, I.A. Tomilin, Thermochim. Acta 280–281 (1996) 303.
[21] N.X. Sun, K. Zhang, X.H. Zhang, X.D. Liu, K. Lu, Nanostruct. Mater. 7 (1996) 637.
[22] F. Ye, K. Lu, J. Non-Cryst. Solids 262 (2000) 228.
[23] E. Illekova, Thermochim. Acta 280/281 (1996) 289.
[24] Y.F. Ouyang, L.Y. Wang, H.M. Chen, X.Y. Cheng, X.P. Zhong, Y.P. Feng, J. Non-Cryst. Solids 354 (2008) 5555.
[25] J.W. Christian (Ed.), The Theory of Transformation in Metals and Alloys, Pergamon, Oxford, 1975.
[26] X.D. Hui, J.L. Yu, M.L. Wang, W. Pong, G.L. Chou, Intermetallics 14 (2006) 931.
[27] X.Q. Zhang, Z.Q. Hu, J. Xu, Mater. Sci. Eng. A 381 (2004) 299.
[28] A.K. Sinha, R.A. Buckley, W. Hume-Rothery, J. Iron Steel Inst. 205 (1967) 191.